

SPECTROSCOPY OF BROAD ABSORPTION LINE QUASARS AT $3 \lesssim z \lesssim 5$: SAMPLE, OBSERVATIONS, AND RESULTS

WEIMIN YI^{1,2,10}, WENWEN ZUO³, JINYI YANG^{7,8}, FEIGE WANG^{6,8}, JOHN TIMLIN², NATHEN NGUYEN⁹, XUE-BING WU^{4,8},
TINGGUI WANG⁵, XIAOHUI FAN⁷, JIN-MING BAI^{1,10}

Draft version April 12, 2019

ABSTRACT

Our knowledge of high redshift, broad absorption line (BAL) quasars (QSOs) remains limited due to their apparent deficiency in the QSO population. We present an observational study of 22 BAL QSOs at $3 \lesssim z \lesssim 5$ based on optical/near-IR spectroscopy, which delivers the largest such sample ever studied in the redshift range. The near-IR spectroscopy covers the H β and/or Mg II broad emission lines for these quasars, allowing us to estimate their central black hole (BH) masses in a robust way. In a subset consisting of seven strong BAL QSOs, we see the prevalence of weak [O III] emission and large C IV broad emission-line (BEL) blueshift ($\sim 3200 \text{ km s}^{-1}$). In another subset consisting of thirteen BAL QSOs having simultaneous observations in Mg II and H β , we found a strong correlation between 3000 Å and 5000 Å continuum luminosity, consistent with previous non-BAL QSO studies; however, there is no correlation between the FWHM of Mg II and H β , possibly due to the effects of strong nuclear outflows traced by BALs and/or C IV-BEL blueshifts. In combination with additional two low-ionization BAL (LoBAL) samples at $1 < z < 2.5$ and $0.5 < z < 1$, respectively, we investigate the cosmological evolution of the LoBAL population at $0.5 \lesssim z \lesssim 5$. There is an increasing trend in Eddington ratio with increasing redshift, while the BH mass distribution appears to peak at $3 < z < 4$ in the augmented LoBAL sample, indicative of a “special” evolution phase, in which nuclear outflows may play an important role in shaping their broad/narrow emission-line regions as well as regulating the growth of their central BHs.

Subject headings: Quasar: broad absorption line: general - quasars: supermassive black holes

1. INTRODUCTION

Broad absorption line quasars (BAL QSOs, Weymann et al. 1991) consist of about 20% up to $\sim 40\%$ of the quasar population before/after correcting selection effects (e.g., Hewett & Foltz 2003; Trump et al. 2006; Gibson et al. 2009; Allen et al. 2011). They provide abundant and powerful diagnostics for observational studies of intrinsic outflows from low to high redshifts via X-ray, UV, optical, and IR spectroscopy. In general, most BAL QSOs are characterized by high-ionization broad absorption lines (HiBALs). A small fraction ($\sim 10\%$, e.g. Trump et al. 2006) of the BAL population also shows absorption troughs characterized by low-ionization species (e.g., Mg II and Al III) in their spec-

tra in addition to HiBALs, which are classified as LoBALs. An even rarer type of BALs show prominent Fe II and Fe III absorption in addition to other low-ionization species, namely FeLoBALs.

BAL phenomena are widely interpreted by either an orientation or evolution effect. The orientation scenario is plausible for most HiBALs due to their similar continuum and emission-line properties (e.g., Weymann et al. 1991; Reichard et al. 2003b). However, spectropolarimetry studies suggest that BAL QSOs seem not to be simply normal quasars seen from an edge-on perspective (e.g., DiPompeo et al. 2010). On the other hand, the evolution scenario has often been proposed for interpreting the phenomena of (Fe)LoBALs¹¹, as they are often found from far-IR luminous and high star-formation objects (e.g., Becker et al. 2000; Farrah et al. 2010). In addition, Gallerani et al. (2010) found systematic differences between BAL and non-BAL QSOs regarding observational properties that should be isotropic. Therefore, BAL QSOs could be used to investigate the early stage of quasar evolution (Boroson & Green 1992; Voit et al. 1993; Becker et al. 2000; Gallerani et al. 2010). In this picture, a LoBAL QSO may be a young AGN in a short-lived transition phase between an ultra-luminous infrared galaxy (ULIRG) and a normal unobscured quasar, which means it could be ignited at some point and blows off dust envelope by powerful outflows since it was accreting material at a high rate. As a consequence, such outflows may quench star formation in the host galaxy (Farrah et al. 2012; Faucher-Giguère et al. 2012).

¹¹ Hereafter, we use (Fe)LoBAL to represent a sample including both FeLoBAL and LoBAL types.

E-mail: wuy34@psu.edu

¹ Yunnan Observatories, Kunming, 650216, China

² Department of Astronomy & Astrophysics, The Pennsylvania State University, 525 Davey Lab, University Park, PA 16802, USA

³ Shanghai Astronomical Observatory, Shanghai 200030, China

⁴ Department of Astronomy, Peking University, Yi He Yuan Lu 5, Hai Dian District, Beijing 100871, China

⁵ CAS Key Laboratory for Research in Galaxies and Cosmology, Department of Astronomy, University of Science and Technology of China, China

⁶ Department of Physics, University of California, Santa Barbara, CA 93106-9530, USA

⁷ Steward Observatory, The University of Arizona, 933 North Cherry Avenue, Tucson, Arizona 85721-0065, USA

⁸ Kavli Institute for Astronomy and Astrophysics, Peking University, Beijing 100871, China

⁹ Departamento de Astronomía de la Universidad de Chile

¹⁰ Key Laboratory for the Structure and Evolution of Celestial Objects, Chinese Academy of Sciences, Kunming 650216, China

TABLE 1
NEAR-IR SPECTROSCOPIC STUDIES OF BALQSOs AT $z \gtrsim 3$

Reference	z range	R	Num
Maiolino et al. (2004)	$4.9 < z < 6.2$	~ 50	2/4
Gallerani et al. (2010)	$3.9 < z < 6.2$	50-800	*/11
Yi et al. (2017)	$z = 4.82$	~ 350	1/1
Wang et al. (2018)	$z = 7.02$	~ 4000	1/1
This work	$2.5 < z < 5.1$	~ 2700	9/16

NOTE. — Previous spectroscopic studies of BALQSOs at high redshift. The Num column represents LoBAL / total BAL QSOs, respectively. The star symbol notes that the LoBAL-type quasars are unidentifiable in that reference.

Systematic studies of large BAL QSO samples have greatly improved our understanding of BAL structures, dynamics and intrinsic physics from high- to low-ionization species (e.g., Reichard et al. 2003a; Gibson et al. 2009; Schulze et al. 2017). BAL QSOs usually exhibit redder continua compared with non-BAL QSOs, which is often interpreted as stronger reddening by dust in the circumnuclear region (e.g., Brotherton et al. 2001; Reichard et al. 2003b). There is, however, an obvious deficiency of sample investigations of higher-redshift BAL QSOs based on UV/optical spectroscopy in the rest frame (see Table 1), leading to poor understanding of the BAL population in the early universe. The extinction curve of BAL QSOs at $z > 4$, based on two dedicated studies (Maiolino et al. 2004; Gallerani et al. 2010), is likely deviated from the SMC extinction curve, supporting the argument of an evolutionary explanation for reddened BAL QSOs at high redshift; in specific, the dust production mechanism in the early universe may differ from that at low or intermediate redshift. However, the above two studies of high- z BAL QSOs mainly focused on the investigation of internal extinction and did not involve in estimating BH masses in their samples (also limited by their low-resolution spectra).

At high redshift, the single-epoch spectral relation is often adopted to investigate supermassive black hole (SMBH) resided in QSOs (e.g., McLure & Dunlop 2004; Vestergaard & Peterson 2006). In this relation, broad emission lines (BELs), such as $H\beta$, $H\alpha$ and Mg II, are considered to be better estimators than the C IV emission line. Since BAL QSOs have strong reddening and significant absorption, which directly affects either the BELs or the neighboring continuum, previous sample investigations of SMBHs in high-redshift QSOs are mainly focused on non-BAL QSOs (e.g., Netzer et al. 2007; Jiang et al. 2007; Trakhtenbrot et al. 2011; Zuo et al. 2015; López et al. 2016; Coatman et al. 2017). Recently, a dedicated spectroscopic study based on a sample of 22 LoBAL QSOs at $1 < z < 2.5$ reveals that line profiles of $H\beta$ and $H\alpha$ are little affected by absorption (Schulze et al. 2017), indicating that they can serve as ideal BH mass estimators for BAL QSOs. Particularly, the spectral region around the $H\alpha$ or $H\beta$ BEL is much less affected by intrinsic reddening and absorption compared to that around the C IV or Mg II BEL. Therefore, the Balmer ($H\alpha$ or $H\beta$) BELs are ideal tracers for the investigation of central engines powering BAL QSOs.

In this work, we present a spectroscopic study from a uniform sample including 22 BAL QSOs at $3 \lesssim z \lesssim 5$. We have obtained near-IR spectra for all of our targets

from the Telescope Access Program (TAP), which allows us to: (1) obtain uniform distributions of BH mass and Eddington ratio for the sample; (2) investigate similarities and differences between the BAL and non-BAL population at high redshift, particularly in a statistical sense; (3) investigate the redshift evolution of the BAL population in conjunction with low- z BAL QSOs. Throughout this paper, a flat cosmology with $H_0 = 70 \text{ km s}^{-1} \text{ Mpc}^{-1}$, $\Omega_M = 0.3$ and $\Omega_\Lambda = 0.7$ is adopted unless stated otherwise.

2. SAMPLE SELECTION AND OBSERVATION

2.1. Sample selection

We have started an observational program since 2016, aiming to probe the central engines among these quasars with the presence of strong BAL troughs that are potentially associated with powerful ionized outflows. In the first stage, we searched for luminous BAL QSOs from the DR12 quasar catalog (Pâris et al. 2017) with $\text{AI}(\text{CIV}) \gtrsim 8000$ at $z > 4.3$. To reliably measure the trough width and depth, quasars with apparent overlapping troughs and significant reddening blueward of the C IV emission line were excluded. Four BAL QSOs remained after this selection. Furthermore, we include another two newly discovered BAL QSOs at $z > 4$, which have been reported from recent studies (Yi et al. 2015; Wang et al. 2016), we also added them to the list of near-IR spectroscopic observations.

Due to the rarity of high- $\text{AI}(\text{CIV})$ BAL QSOs at $z > 4$, we added some BAL QSOs showing relatively strong BAL troughs ($\text{AI} > 2000$) and several comparison QSOs with relatively weak BAL troughs ($\text{AI} < 2000$) at $2.5 < z < 4$ into our observational list in the second stage. Considering strong telluric-absorption windows in the near-IR wavelengths (i.e., 1.35–1.45 μm and 1.8–1.9 μm), a proper redshift cut was made to keep the Mg II and/or $H\beta$ emission lines away from these windows. This leaves us 11 BAL QSOs at $2.5 < z < 4$. Together with the 6 BAL QSOs at $4.3 < z < 5$ from the first stage and another 5 BAL QSOs at $3 < z < 4$ from Zuo et al. (2015), our final sample consists of 22 BAL QSOs with newly and previously obtained near-IR spectra.

Interestingly, we found that at least 12 quasars in the sample are LoBAL QSOs based on our analyses of their optical/near-IR spectra. To better understand the LoBAL population in a statistical sense, we construct a LoBAL sample in combination with additional two LoBAL samples at $z < 0.8$ and $1 < z < 2.5$, respectively, to investigate their properties and redshift evolution in this BAL-subtype population (see Section 4.2.1).

2.2. Compilation of optical data

Our optical spectra in the sample are mainly obtained from the DR14 SAS website¹² by matching the coordinates of the selected BAL quasars to source positions within a $3''$ tolerance. These spectra are corrected for calibration errors that result from atmospheric differential refraction and fiber offsets during observations (see Margala et al. 2016 for details).

Additional spectroscopic observations were carried out during several runs from 2015 to 2018 using the Yunnan

¹² <https://dr14.sdss.org/optical/spectrum/search>

TABLE 2
MEASUREMENTS OF BAL QSOs BY OPTICAL SPECTROSCOPY

Name	RA (J2000)	DEC (J2000)	AI(CIV) (km s^{-1})	v_{min} (km s^{-1})	v_{max} (km s^{-1})	v_{cen} (km s^{-1})	EW (\AA)	d_{BAL}	z	Type
014049.18–083942.5	25.20492	−8.66181	1760	23134	28496	25857	11.9	0.42	3.717	Hi
015048.83+004126.2	27.70346	0.69061	538	2913	4005	3470	3.4	0.57	3.701	Hi
021646.94–092107.3	34.19561	−9.35204	2697	11695	23009	13740	19.4	0.58	3.732	Hi
074628.70+301419.0	116.61961	30.23863	11060	7016	30120	9600	68.1	0.81	3.173	Lo
APM08279	127.92375	52.75486	1276	4125	10607	7587	10.0	0.29	3.911	Hi
083718.63+482806.5	129.32764	48.46848	8068	2645	15299	8141	48.3	0.73	3.64	Lo
084401.95+050357.9	131.00813	5.06608	9173	4656	28197	13935	59.2	0.48	3.36	Lo
091935.36+193834.7	139.89737	19.64297	13189	1077	22360	10304	79.2	0.71	3.541	Lo
103256.70+514014.5	158.23628	51.6707	11018	1231	27751	9989	69.6	0.62	3.925	Lo?
115023.57+281907.4	177.59825	28.31875	788	1109	2549	1832	4.92	0.63	3.12	Hi
120447.15+330938.7	181.19647	33.16077	12430	6048	29166	16577	76.3	0.63	3.652	Lo
121027.62+174108.9	182.61508	17.68581	6484	14122	29000	20965	41.8	0.5	3.831	Lo
123754.82+084106.7	189.47844	8.68522	2938	1612	6109	3710	17.5	0.74	2.897	Hi
125958.72+610122.9	194.99469	61.02303	478	3375	4941	4238	3.76	0.39	3.572	Hi
141546.24+112943.4	213.94267	11.49540	4896	3209	13804	7533	31.3	0.56	2.556	Lo
150332.17+364118.0	225.88404	36.68833	4387	3924	28213	5232	32.3	0.76	3.261	Lo
012247.34+121624.0	20.69730	12.27330	14360	5886	30479	14438	76.1	0.68	4.82	Lo
092819.28+534024.1	142.08037	53.67337	9711	8035	27634	9445	59.7	0.85	4.47	Lo
104846.63+440710.7	162.19431	44.11966	12258	4820	25899	13520	74.3	0.67	4.39	Lo
133529.45+410125.9	203.87271	41.02388	5143	16436	26873	20803	32.0	0.59	4.3	Lo
151035.29+514841.0	227.64705	51.81141	6790	5160	21578	5749	43.0	0.77	5.096	Lo?
163810.38+150058.2	249.54325	15.01617	5030	21700	32700	26850	31.7	0.55	4.84	Lo?

NOTE. — CIV-BAL properties of 22 BAL QSOs in the sample. v_{cen} is a flux-weighted centroid velocity in the CIV-BAL trough; v_{min} and v_{max} are the corresponding minimum and maximum velocities, respectively. Hi/Lo represent high-/low-ionization BALs, respectively. The Lo? symbol represents an unidentifiable LoBAL due to the lack of wavelength coverage or strong contamination from telluric absorption.

Faint Object Spectrograph and Camera mounted on the Lijiang 2.4m telescope (LJT/YFOSC, Fan et al. 2015). Considering FWHM of the YFOSC imaging data varies mostly in the range from $1.0''$ to $2.5''$, we thus chose a slit of $1.8''$ in the spectroscopic observations. Each night the Neon/Helium arc lamps were taken for wavelength calibration and a spectrophotometric standard star was observed followed by the target at similar airmass and position for flux calibration. All the calibration data, including bias, sky-flat fields, and internal lamp flats were obtained at the beginning/end of each observing night. The data reduction was performed by IRAF packages following the standard reduction steps for bias/sky subtractions, flat-fielding and flux calibration.

Basic descriptions of these BAL QSOs are tabulated in Table 2, where most of these measurements are retrieved from Pâris et al. (2017). The systemic redshift values are determined by the [O III], H β , or Mg II line from near-IR spectra, depending on their appearance. We visually inspected all spectra before performing quantitative measurements.

2.3. Near-IR spectroscopic observations and data reduction

The near-IR spectroscopic observations of all objects tabulated in Table 2 were carried out by the TripleSpec (Wilson et al. 2004) at the Palomar Hale 200 inch telescope (P200/TripleSpec, Wilson et al. 2004). TripleSpec provides a wide wavelength coverage from $0.95 \mu\text{m}$ to $2.46 \mu\text{m}$ at an average spectral resolution of $R \sim 2700$, allowing simultaneous observations in the JHK bands. High Fowler depth ($6 \sim 10$) is set for faint objects to optimize the readout noise after each single exposure. A slit width of $1''$ and the ABBA dither pattern along the slit were chosen to improve the sky subtraction for all tar-

gets throughout these observational runs. Total exposure times varied between 24 and 60 minutes, depending on the apparent magnitudes and weather conditions. During each night, several telluric A0V standard star were observed at a similar airmass compared to that of the target.

The data reduction for the spectroscopic data from TripleSpec is processed using the modified IDL-based Spextool3 package (Cushing et al. 2004), as described in detail from Zuo et al. (2015). The standard process includes sky background subtraction, flat field correction, wavelength identification and telluric correction. Based on the reduced near-IR spectra, we then determine systemic redshift using the [O III], or H β , or Mg II emission line, ordered by a descending priority when available.

2.4. Notes for individual objects

J0122+1216 was discovered as a quasar using the Lijiang 2.4-m Telescope (Yi et al. 2015) in optical spectroscopy; later, it was further identified as a LoBAL QSO at $z = 4.82$ in near-IR spectroscopy (Yi et al. 2017). Recently, this LoBAL QSO was also reported from Jeon et al. (2017), where their measurements of the luminosity and BH mass are consistent with those from Yi et al. (2017). Noticing the quality of near-IR spectra obtained by the Magellan telescope (see Jeon et al. 2017) is much higher than that from Yi et al. (2017), we use their near-IR spectra (in private communication) for J0122+1216 in this work.

APM08279 is one of the brightest quasars caused by gravitational lensing (Irwin et al. 1998). J1415+1129 is another lensed quasar having a ‘‘cloverleaf’’ structure (Magain et al. 1988). Since previous studies reported a wide range of possible magnification factors ($4 \sim 100$) for this quasar, for simplicity, we choose to use the corrected

bolometric luminosity assuming that it is equal to the Eddington luminosity limit.

The basic properties of the sample are tabulated in Table 2, in which high- and low-ionization BAL types are marked. In total, we identified twelve LoBAL QSOs. Another three cannot be identified due to low S/N spectra and/or an incapability of identifying low-ionization BALs in strong telluric-absorption windows.

3. SPECTROSCOPIC MEASUREMENTS AND ANALYSES

Several methods have been applied to get more reliable measurements based on optical/near-IR spectroscopic/photometric data, including redshift determination, similar spectral shape matching at close redshifts, continuum fitting, correction of absolute spectral flux, and emission line fitting. The related results are tabulated in Table 2 and Table 3.

3.1. Measurements from optical spectra

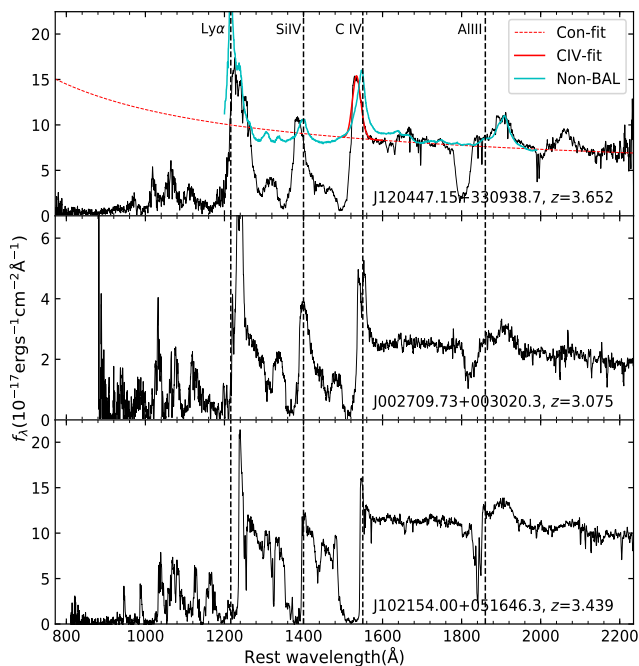


FIG. 1.— The top panel demonstrates continuum (red dashed) and non-BAL template (cyan) fits. The red solid line is a Gaussian fit of the C IV line. The middle/bottom panels show the matched spectra with similar redshift, Al(C IV), and spectral shape.

Similar to previous studies (e.g., Filiz Ak et al. 2013; Grier et al. 2016; Yi et al. 2019), we adopt a reddened power-law model to fit the continuum emission with a nonlinear least-squares fitting algorithm. We modeled the continuum in each spectrum using a SMC-like reddened power-law function from Pei (1992) with three free parameters including the amplitude, power-law index, and extinction coefficient. The initial continuum-fit windows are composed of relatively line-free (RLF) regions. However, these default windows do not always reasonably sample the continuum for all quasars in the sample, so they are adjusted where necessary to reach an acceptable fit. In particular, apparent emission/absorption lines exhibiting in the default windows among all spectra have been excluded.

We masked these pixels flagged by “and-mask” from SDSS pipeline before the continuum fit. All spectra are then converted to the rest frame using the redshifts determined by the [O III], H β , or Mg II line from the near-IR spectra. Some emission and/or absorption features appear to be frequently present in the same fitting regions. Therefore, we adopt a sigma-clipping algorithm that consists of fitting the reddened power-law function to the RLF windows for each spectrum, and then rejecting data points that deviate by more than 3σ from the continuum fit for each pixel in each window. The final continuum fit is obtained by re-fitting the remaining data points. We do not attach physical meaning to the values of $E(B - V)$ derived from our fits since there is a degeneracy between the UV spectral slope and intrinsic reddening. The uncertainty of the continuum fit is obtained via a Monte Carlo approach through randomizations of spectral errors in the RLF windows. Then, quantities such as Al(C IV), minimum/maximum trough velocities, and, EW etc, are measured based on the reddened power-law fits (see Table 2).

3.2. Flux calibration of near-IR spectra

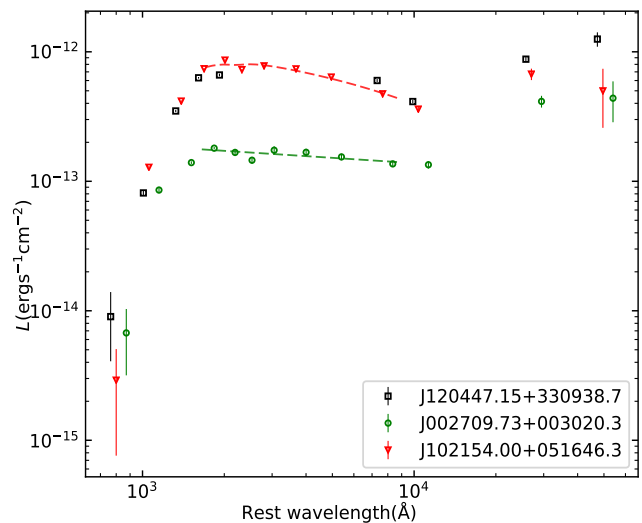


FIG. 2.— SEDs of the three quasars constructed from SDSS, UKIDSS and WISE photometric magnitudes. The dashed lines show reddened power-law (red) and power-law (green) fits for the two matched quasars between 1600Å to 9000 Å.

The near-IR spectroscopic observations were carried out under non-photometric conditions. In addition, the cross-dispersion mode of spectroscopy may lead to a large uncertainty for near-IR spectral flux calibration, thus an absolute flux calibration is required for reliable measurements of QSO properties, such as luminosity, BH mass, and Eddington ratio. Since quasars usually show less variability at redder wavelengths, we simply tied the absolute flux of near-IR spectral continua to the 2MASS or UKIDSS photometric magnitudes if they are available. However, the photometric magnitudes of some objects in this sample are not found from UKIDSS or 2MASS. Therefore, an alternative of flux calibration is required for these objects, which is described as follows:

1. We match optical spectra within a similar range

of AI(C IV) and redshift from the DR12 BAL QSO catalog.

2. BAL QSOs without footprints in the 2MASS or UKIDSS catalog are excluded.
3. Visual inspection is followed to further select these BAL QSOs with similar spectral shapes and features to the targets in our sample.

As an example demonstrated in Figure 1, there are two BAL QSOs chosen as a reference for the continuum fit. SEDs in the two matched BAL QSOs appear to be redder than non-BAL QSOs, most likely due to intrinsic reddening and Ly α -forest absorption at high redshift. We only account for the local SED fit between 1600 and 10000 Å in the rest frame, where a power-law or reddened power-law continuum shape is expected. For the two reference QSOs, they can be well fitted by the power-law and reddened power-law models, respectively (see Figure 2). A longer wavelength cut is necessary since the hot-dust reprocessing starts to dominate the QSO SED at $\lambda > 10000$ Å. Finally, we fit the local SED of our target using the same models that are applied to the SED fitting process of the matched quasars in the same wavelength range, and their differences are taken as propagated uncertainties for the placement of the continuum. As the uncertainty is dominated by the above procedures, we did not account for additional uncertainties, such as the uncertainty generated from Monte Carlo simulations.

In general, we found that the 5100 Å flux density derived from a power-law fit is quite close to that from a reddened power-law fit while a larger deviation may appear at 3000 Å in the sample using the two models. Thus, the continuum placement at 5100 Å is our preferential choice for the conversion to the bolometric luminosity using the nominal factors (5.18 for 3000 Å and 9.26 for 5100 Å, respectively; see Shen et al. 2011). Finally, the absolute flux calibration is corrected by the Galactic extinction using $R_V = 3.1$ Milky Way extinction model (Cardelli et al. 1989) and a corresponding A_V value (Schlafly et al. 2011).

3.3. The emission-line measurements

Emission line properties are measured by fitting the local regions around the H β and/or Mg II emission lines with a pseudo continuum+line model (see inset panels in Figure 3). Strong telluric-absorption windows are masked out in the near-IR spectra before fitting. For consistency, we adopt a similar method of continuum fitting and emission-line modeling from Schulze et al. (2017), which is illustrated as follows:

1. The continua around Mg II and H β emission lines are fitted by the model including a power-law (PL) function+optical/UV Fe II templates (Boroson & Green 1992; Salvander et al. 2007). We do not consider the Balmer continuum in this work.
2. The broad emission-line fitting is then based on the pseudo-continuum subtracted spectrum. Specifically, no more than three broad and one narrow Gaussians are adopted to fit broad emission lines. We mask out absorption troughs during the fitting

around the Mg II emission-line if its profile is obviously affected by these troughs.

3. Due to the weakness of the [O III] emission line in the sample and spectral quality, the [O III] emission line is fitted by one Gaussian for most quasars in the sample. The upper limit on FWHM of the [O III] emission line is set by 2000 km s^{-1} to account for possible broad [O III] components that may be associated with outflows.
4. Since the widely used Boroson & Green (1992) template may fail to provide a satisfactory Fe II fit for all spectra, following Bischetti et al. (2017), we add additional two Gaussians during the fit for those objects with strong Fe II emission at ~ 4940 Å and ~ 5040 Å, respectively.

The upper limit on the velocity width (2000 km s^{-1}) used for the [O III] line fit is obviously larger than the typical velocity width ($< 900 \text{ km s}^{-1}$) of narrow emission lines (NELs). However, this upper limit is reasonable since signatures of NEL outflows appear to be common in the luminous quasar population, particularly at high redshifts (e.g., Netzer et al. 2004; Harrison et al. 2014; Bischetti et al. 2017). The wavelength separation between the [O III] $\lambda 5007$ and [O III] $\lambda 4960$ component has been constrained to the range from 45 Å to 50 Å in the rest-frame, with a ratio of their normalizations equal to 1:3. In addition, based on the quality of these near-IR spectra, we use only one Gaussian to fit the [O III] emission line for the majority in the sample except for two objects (J1259+6101 and J1415+1129, see Figure 4). Following a similar procedure from Bischetti et al. (2017), we introduced additional Gaussians to account for strong emission features (likely caused by Fe II emission) observed at ~ 4940 and ~ 5040 Å for three objects (J0837+4828, J0844+0503, J1259+6101, see Figure 4) in the sample. For the measurement of FWHM of the H β emission line, we consider all broad Gaussians (up to three components) during the fitting process.

Spectral fits around the Mg II emission line, however, are more challenging due to various reasons. First, there is no available Mg II-based size-luminosity relation compared to that derived from the H β line from reverberation mapping campaigns (e.g., Kaspi et al. 2000; Bentz et al. 2013), indicating the measurement of the Mg II line less reliable than that of the H β line. Second, the Mg II line profile is potentially affected by absorption in our sample, especially for these objects showing deep and wide C IV-BAL troughs. Although the Mg II-BAL troughs are generally weaker and narrower than those found in C IV, they are often attached on the Mg II emission-line profile, making their identifications more difficult than those of C IV-BAL troughs. Third, Popovic et al. (2019) reported that the Mg II broad emission line appears to originate from two subregions: one contributes to the line core that is probably virialized, and the other is associated with an emitting region characterized with outflows and inflows nearly orthogonal to the disc, which mostly contributes to the emission of the Mg II broad line wings. Fourth, whether or not considering the narrow component during the Mg II line

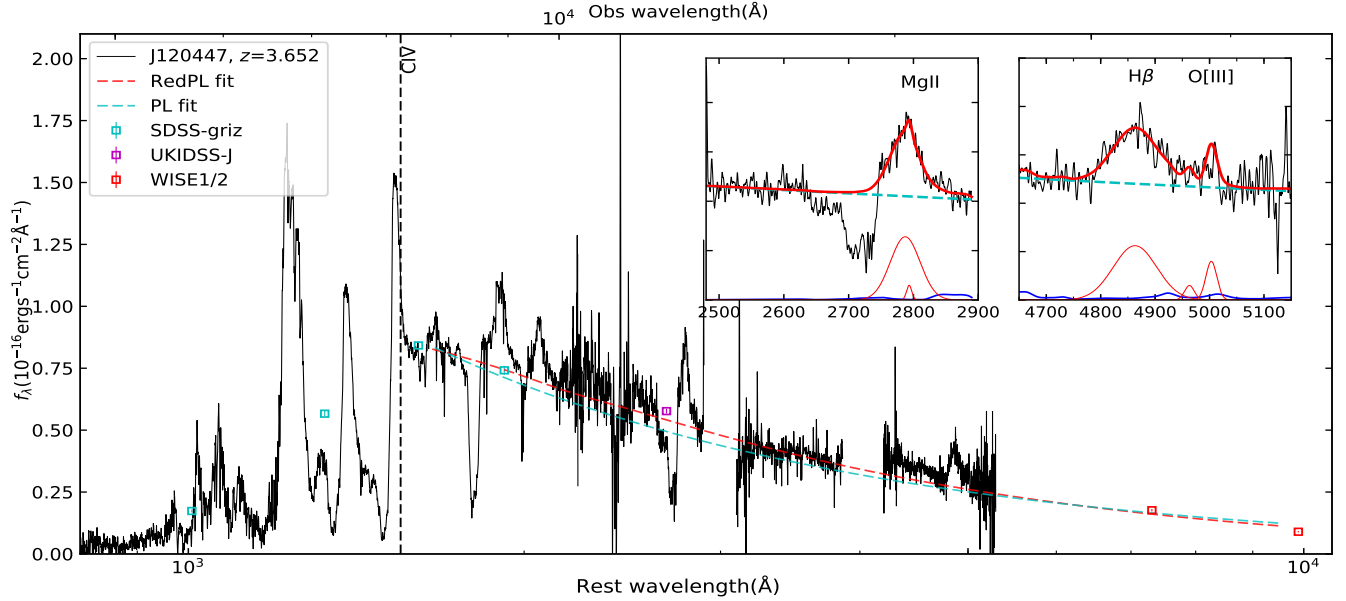


FIG. 3.— An example of the SED fit using power-law (PL) and reddened PL functions, respectively, based on photometric (cyan and red squares) data; black dashed line show an apparent blueshift compared to the systemic redshift determined by the [O III]5007 emission line. The cyan, magenta, and red squares represent photometric data from SDSS, UKIDSS, and WISE, respectively. Inset panels show spectral fits around the Mg II and H β emission lines. The cyan dashed lines represent the power-law fit for the continuum, blue lines depict the fitted UV/optical Fe II components, and the thin red lines represent all broad and narrow Gaussians for the fits around Mg II, H β and [O III] emission lines.

TABLE 3
SPECTRAL MEASUREMENTS AND DERIVED BLACK HOLE PROPERTIES BASED ON P200/TRIPLESPEC OBSERVATIONS

Name SDSS J	FWHM _{MgII} (km s ⁻¹)	log $L_{3000\text{\AA}}$ (erg s ⁻¹)	FWHM _{Hβ} (km s ⁻¹)	log L_{5100} (erg s ⁻¹)	FWHM _[OIII] (km s ⁻¹)	log L_{bol} (erg s ⁻¹)	log M_{BH} (M_{\odot})	log λ
0140+0839	4735 ± 2430	47.25 ± 0.01	5348 ± 697	46.99 ± 0.01	1870 ± 500	47.96 ± 0.01	9.86 ± 0.11	-0.02 ± 0.12
0150+0041	5668 ± 105	46.95 ± 0.01	5225 ± 780	46.74 ± 0.01	1410 ± 80	47.71 ± 0.01	9.38 ± 0.12	0.01 ± 0.13
0216+0921	2550 ± 650	46.99 ± 0.03	3729 ± 80	46.77 ± 0.03	-	47.74 ± 0.01	9.38 ± 0.03	0.25 ± 0.05
0746+3014	4517 ± 2078	47.13 ± 0.09	7018 ± 900	46.90 ± 0.01	1300 ± 360	47.87 ± 0.01	10.05 ± 0.19	-0.29 ± 0.19
APM08279	-	-	5020 ± 38	46.92 ± 0.5	-	47.89 ± 0.5	9.80 ± 0.30	0.001 ± 0.30
0837+4828	4244 ± 260	46.83 ± 0.08	5197 ± 1630	46.63 ± 0.03	1436 ± 240	47.59 ± 0.03	9.65 ± 0.25	-0.17 ± 0.23
0844+0503	3850 ± 830	47.44 ± 0.01	5812 ± 35	47.25 ± 0.01	2100 ± 90	48.21 ± 0.01	10.06 ± 0.01	0.03 ± 0.03
0919+1938	3800 ± 1690	46.82 ± 0.1	5214 ± 380	46.70 ± 0.03	1400 ± 690	47.67 ± 0.03	9.70 ± 0.07	-0.14 ± 0.11
1032+5140	-	-	3193 ± 820	46.63 ± 0.02	-	47.59 ± 0.02	9.23 ± 0.21	0.25 ± 0.32
1150+2819	6024 ± 5450	47.24 ± 0.02	4071 ± 60	47.02 ± 0.02	1069 ± 35	47.99 ± 0.02	9.64 ± 0.02	0.24 ± 0.04
1204+3309	4928 ± 188	46.93 ± 0.04	5785 ± 165	46.88 ± 0.02	1400 ± 560	47.84 ± 0.02	9.87 ± 0.03	-0.14 ± 0.04
1210+1741	-	-	6476 ± 960	47.07 ± 0.01	-	48.04 ± 0.01	10.07 ± 0.04	-0.14 ± 0.05
1237+0841	4840 ± 2030	47.10 ± 0.01	-	-	-	47.81 ± 0.01	9.77 ± 0.4	-0.07 ± 0.4
1259+6101	2400 ± 4000	46.99 ± 0.01	5540 ± 2250	46.83 ± 0.01	1680 ± 310	47.80 ± 0.01	9.81 ± 0.22	-0.13 ± 0.24
1415+1129	4593 ± 900	46.71 ± 0.03	3915 ± 125	46.49 ± 0.03	1390 ± 86	47.46 ± 0.03	9.66 ± 0.05	0.002 ± 0.18
1503+3641	3428 ± 820	47.20 ± 0.02	5336 ± 62	46.88 ± 0.02	1387 ± 86	47.85 ± 0.02	9.80 ± 0.02	-0.07 ± 0.08
0122+1216	4210 ± 160	46.79 ± 0.04	-	-	-	47.50 ± 0.04	9.47 ± 0.06	-0.1 ± 0.10
0928+5340	4408 ± 190	46.99 ± 0.1	-	-	-	47.70 ± 0.1	9.64 ± 0.06	-0.05 ± 0.06
1048+4407	4162 ± 357	46.97 ± 0.05	-	-	-	47.68 ± 0.05	9.58 ± 0.09	-0.01 ± 0.15
1335+4101	3010 ± 2200	47.06 ± 0.01	-	-	-	47.78 ± 0.01	9.34 ± 0.48	0.315 ± 0.50
1510+5148	4515 ± 2250	46.51 ± 0.05	-	-	-	47.24 ± 0.05	9.43 ± 0.36	-0.31 ± 0.41
1638+1500	3670 ± 970	47.02 ± 0.1	-	-	-	47.74 ± 0.1	9.50 ± 0.25	0.12 ± 0.26

NOTE. — L_{bol} , M_{BH} and λ are derived from the broad H β emission line if available; otherwise, they are estimated by the Mg II emission line.

decomposition may significantly affect the FWHM measurement of the broad Mg II line. Other challenges arise from different recipes of the single-epoch relation used in previous studies, the possibility of Mg II emission-line blueshift (cannot be determined without the aid of H β), and the possibility to correct the Mg II-based BH mass (e.g., Woo et al. 2018) etc., need to be considered as well. Therefore, caveats must be kept in mind when using the Mg II broad line for the BH mass estimation, especially

in the case of very large widths (FWHM > 6000 km s⁻¹, e.g., Yi et al. 2019) and/or in the case of strong blue asymmetry (e.g., Plotkin et al. 2015).

To mitigate the contamination of absorption and reconstruct the Mg II emission line in a reasonable sense, we mask out these absorption regions through visual inspection. The peak position of the Mg II emission line is constrained to the wavelength range between 2796 Å

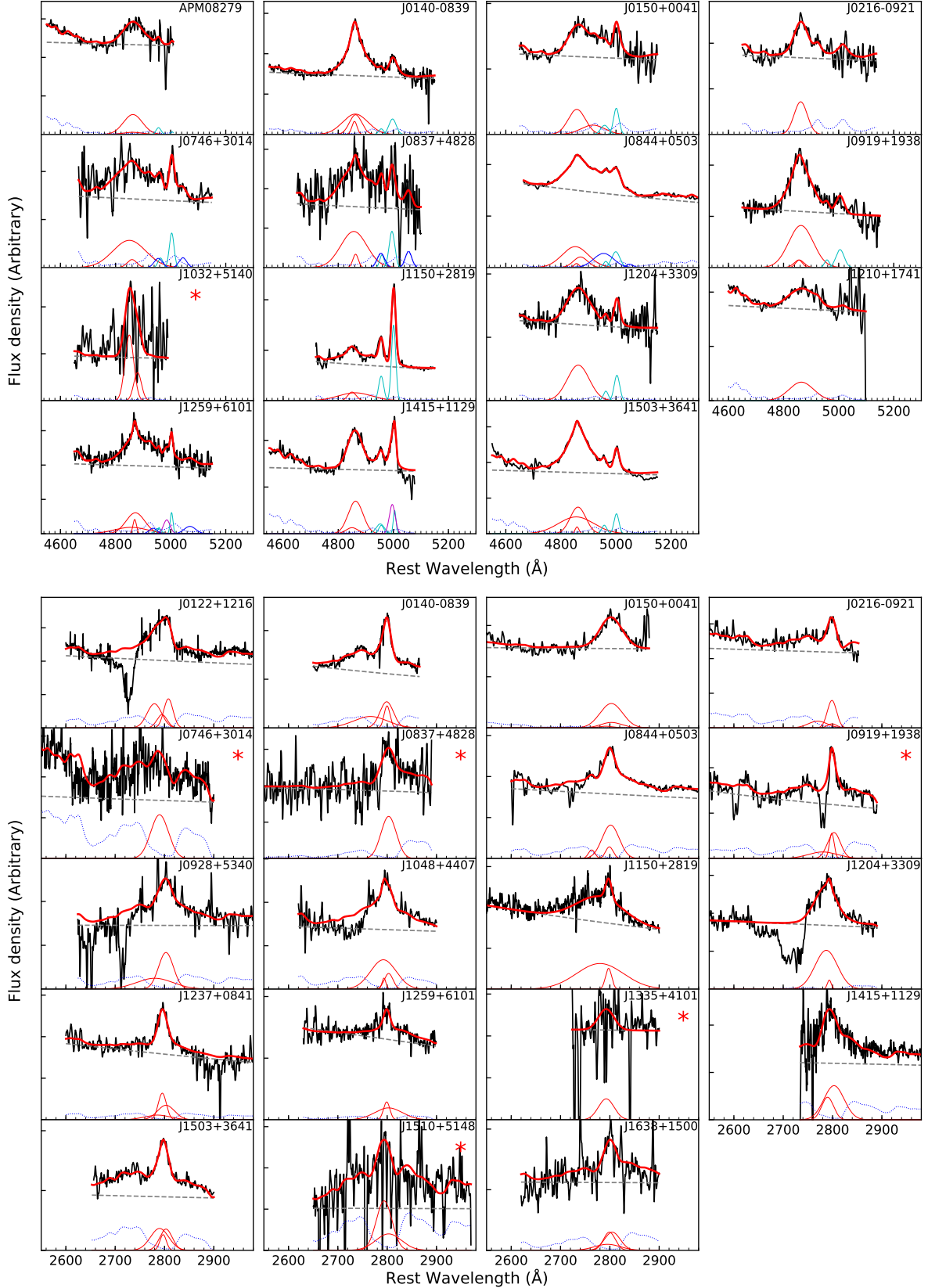


FIG. 4.— Spectral fits around the $H\beta$ (upper panel) and $Mg\ II$ (lower panel) emission lines in our sample. The model of $H\beta$ emission line includes the power-law continuum (grey dashed), optical Fe II template (dotted blue), multiple Gaussians for the broad $H\beta$ line (thin red), the $[O\ III]$ 4960/5008 doublet (cyan and magenta lines, in which magenta lines represent broad FWHM component of the $[O\ III]$ line), and additional two broad Gaussians for Fe II bumps at 4940 \AA and 5040 \AA (blue line) if exist. The model of $Mg\ II$ emission line includes the power-law continuum (grey dashed), UV Fe II template (dotted blue), multiple Gaussians for the broad $Mg\ II$ line (thin red). The red stars in both panels refer to these objects with low S/N spectra and/or absorption attached on the line.

and 2803 Å. No more than three broad and one narrow Gaussian components are taken into account during the Mg II emission-line fit. Since the spectral quality do not allow us to decompose the Mg II line in a reliable way, we did not exclude the narrow component for the FWHM measurement of Mg II, even if it exists in some cases. Therefore, the FWHM of the Mg II emission line is determined by combining all the components (including the narrow Gaussian if it exists) after the spectral fitting.

The whole spectral fitting process for an individual object is demonstrated in Figure 3, in which we scaled the optical/near-IR spectra by a ratio between the synthetic spectroscopic magnitude and the corresponding photometric magnitude. The local SED fits derived from both the power-law and reddened power-law functions are demonstrated by the cyan dashed and red dashed lines, respectively. All the spectral fits around the Mg II and/or H β emission lines in the sample are shown in Figure 4.

3.4. The composite spectrum of strong BAL QSOs

There are 7 QSOs ($\sim 32\%$) in our sample having strong C IV-BAL features (C IV-BAL EW > 60 Å) with an average S/N > 7 at 3000 Å or 5100 Å spectra. All of them exhibit large C IV-BEL blueshifts (> 3000 km s $^{-1}$) with maximum LOS velocities ($v_{max} > 20000$ km s $^{-1}$), which may represent an extreme subtype in the BAL population. Thus, we construct a composite spectrum from these QSOs to investigate similarities and differences in the continuum and emission-line properties compared with the non-BAL QSO composite spectrum from Vanden Berk et al. (2001).

These optical/near-IR spectra used to construct the composite spectrum cover a wide wavelength range from 900 Å to 5200 Å in the rest frame. All the selected spectra are then shifted into rest frame and normalized at 1600 Å for the optical spectra and at 3600 Å for the near-IR spectra. We use the geometric mean among these normalized spectra to produce stacked spectra as shown in Figure 5, where the composite spectra at $900 < \lambda < 1700$ Å (top panel) and $1800 < \lambda < 5200$ Å (bottom panel) are generated by the optical and near-IR spectra, respectively. Since the near-IR spectra of the seven BAL QSOs have different redshifts ranging from 3.179 to 4.82, some breaks may appear due to the cut of telluric-absorption windows.

The BAL composite spectrum shows significant intrinsic reddening at $\lambda < 2000$ Å while it appears to be largely free of intrinsic reddening at $\lambda > 4000$ Å in the rest frame. Moreover, the H β emission-line profile does have a good symmetric shape, confirming that the H β emission line in BAL QSOs can serve as an equally reliable BH estimator as in non-BAL QSOs. On the other hand, the composite spectrum shows an apparently wider profile in the H β emission line compared to the non-BAL QSO template from Vanden Berk et al. (2001), probably signaling an intrinsic difference between the two quasar subtypes.

In good agreement with the finding from Yi et al. (2017), the composite spectrum of strong BAL QSOs reveals striking blueshifts over all high-ionization BELs (~ 3200 km s $^{-1}$ in C IV), implying a potential link between BAL and BEL outflows. Moreover, the composite

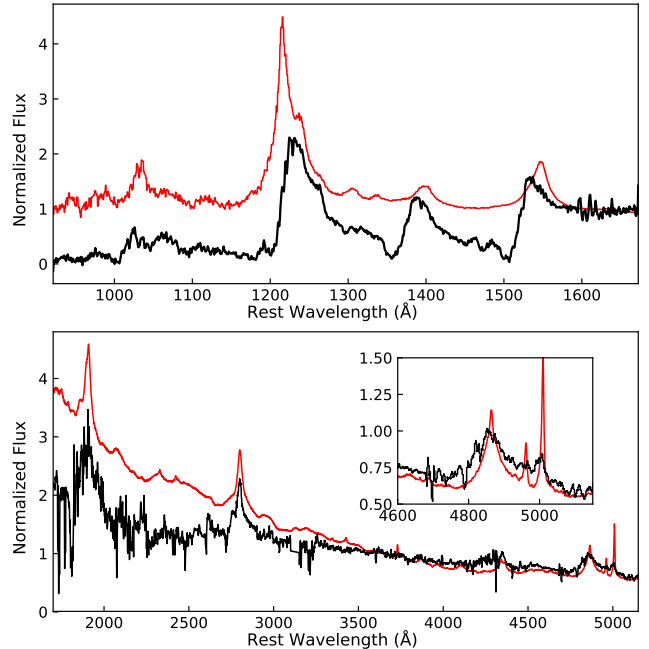


FIG. 5.— The black lines show the composite spectra (smoothed by 20-pixel Boxcar filter) generated from a set of optical/near-IR spectra at $3 < z < 5$, in which a non-BAL QSO template (red) from Vanden Berk et al. (2001) is over plotted as a comparison. spectrum shows significant reddening at $\lambda < 3000$ Å and weak [O III] emission features compared to the non-BAL QSO template. As a comparison, about 25% non-BAL QSOs from Zuo et al. (2015) show comparable weakness of the [O III] emission at similar redshift and luminosity.

Since the observed [O III] and C IV emission lines are good indicators to trace the integration rather than the line-of-sight effect, the prevalence of weak [O III] emission and large C IV blueshift among the strong BAL QSOs disfavors the orientation interpretation for the origin of BAL and non-BAL QSOs; instead, these emission-line features likely support the evolution scenario, where BAL QSOs that are associated with nuclear outflows could be an early-phase or “special-phase” manifestation in the quasar evolution history.

Previous studies found that the [O III] weakness tend to be associated with broad blueshifted C IV emission in samples of Type 1 luminous quasars (e.g., Netzer et al. 2004; Vietri et al. 2018); furthermore, our study of the BAL QSOs at high redshift suggests that the weakness of [O III] emission appears to be more associated with the C IV-BEL blueshift compared to the dependence of luminosity, which deserves a dedicated future work for further investigations.

4. COMPARISON WITH OTHER SAMPLES

In the section, we investigate the distributions of physical properties and compare them with other non-BAL and BAL samples matched in luminosity and/or redshift. We also investigate the redshift evolution of the LoBAL population in conjunction with the other two LoBAL samples at $1 < z < 2.5$ and $z < 1$, respectively.

4.1. Comparison with non-BAL samples at similar redshift and luminosity

Previous studies based on non-BAL quasar samples found that the FWHM distribution of the Mg II BEL is

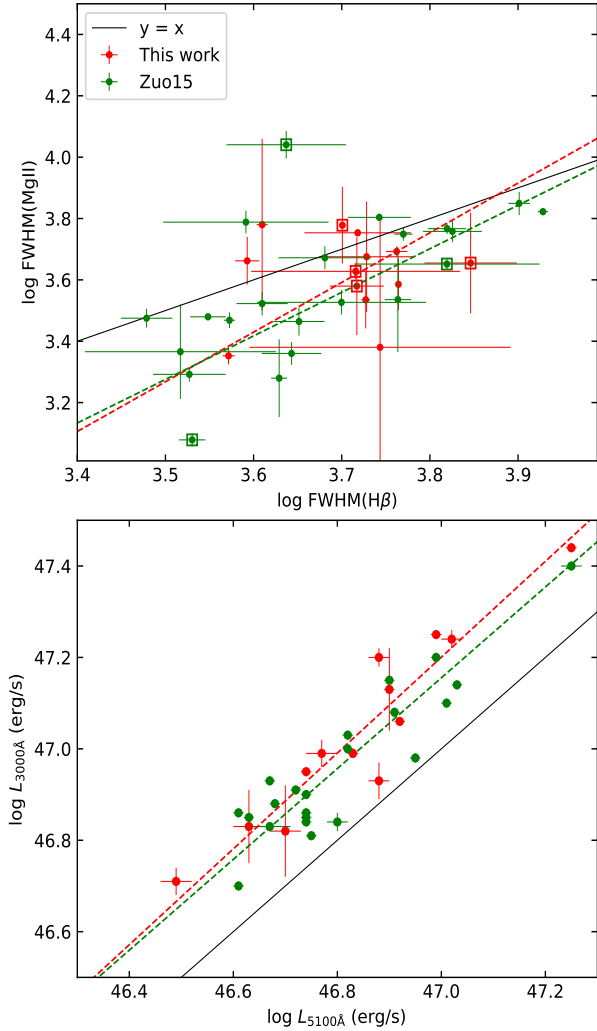


FIG. 6.— Top: FWHMs of Mg II versus H β emission lines. Black line is the 1:1 distribution. The open red/green squares represent these objects with relatively low-quality fitting results from the two samples. Bottom: Distribution of 5100 Å monochromatic luminosity versus 3000 Å monochromatic luminosity. Red and green dashed lines are the linear fits based on the orthogonal distance regression.

(linearly) correlated with that of the H β BEL at a high significance level (e.g., Trakhtenbrot & Netzer 2012; Zuo et al. 2015), thus the Mg II BEL is usually considered as an alternative BH-mass estimator in good agreement with the H β line.

There are 13 objects in our sample having simultaneous observations of the Mg II and H β emission lines, which provide an opportunity to test whether this correlation holds in the luminous BAL QSOs at high redshift. In addition, four quasars (marked by open red squares in the upper panel of Figure 6) in our sample may bias the statistical results, as they have relatively low-S/N spectra and/or broad absorption attached on the Mg II line. We checked the correlation after excluding them, and found the results are consistent with the entire sample of 13 objects via the Spearman test. Therefore, we use the entire sample of 13 objects for the related analyses throughout this section.

The BH mass measurement based on the single-epoch

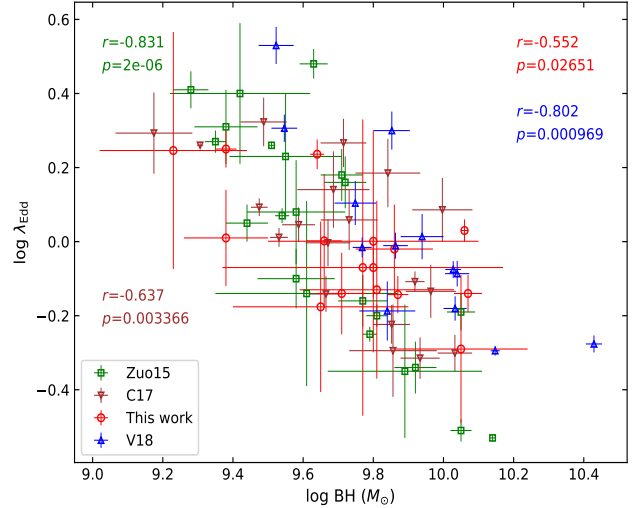


FIG. 7.— Distributions of Eddington ratio versus BH mass, in which the comparison between a subset of the sample (red) and three non-BAL sample within a similar redshift/luminosity range based on the H β estimator at $z < 4$. All the three non-BAL QSO samples show strong correlations compared to a tentative correlation in the BAL sample.

relation is proportional to the square of FWHM, which can dominate the discrepancies of BH masses and Eddington ratios measured by the two different estimators. Thus, it is essential to investigate its distribution and make comparisons with other studies. We choose three non-BAL comparison samples (Zuo et al. 2015, Coatman et al. 2017, and Vietri et al. 2018; hereafter Zuo15, C17, and V18, respectively) matched in luminosity and redshift. The sample of Zuo15 includes 24 non-BAL QSOs in a similar redshift and luminosity range, among which 22 of them have the coverage of both the H β and Mg II emission lines. The near-IR spectra from Zuo15 and our sample were obtained by the same instrument (P200/TripleSpec), largely alleviating uncertainties caused by different instruments for the comparisons. The comparison sample of C17 consists of 230 non-BAL QSOs at $1.5 < z < 4$, from which we select 19 using the thresholds at $z > 2.56$ and $46.5 < \log L_{5100} < 47.3$. Additionally, we select 13 non-BAL QSOs at $z \sim 3.3$ and $\log L_{5100} \sim 47$ from Vietri et al. (2018) to construct the V18 comparison sample.

As shown in the top panel of Figure 6, the distribution of FWHM-Mg II versus FWHM-H β in this work is broadly consistent with that from Zuo et al. (2015) based on the orthogonal distance regression fits (red and green dashed lines are the two fits for the two samples, respectively). In addition, both distributions of the two samples deviate from the one-to-one line (black), with more objects showing FWHM-H β larger than FWHM-Mg II. However, the distribution between the two different broad emission lines in FWHM from our sample appears to be less correlated compared with Zuo15, which is confirmed by quantitative analyses via the Spearman test ($r = -0.09, p = 0.775$ and $r = 0.67, p = 0.0006$ for our sample and Zuo15, respectively). No correlations are found in our sample, which could be associated with strong nuclear outflows traced by BALs and/or C IV emission-line blueshifts.

Conversely, the two samples follow a similar linear re-

lation in the distribution of 5100 Å monochromatic luminosity versus 3000 Å monochromatic luminosity based on the linear fits (see red/green dashed lines in the bottom of Figure 6), although the two samples consist of BAL and non-BAL quasars, respectively. In a quantitative sense, we cannot find significant differences in the distribution of FWHM-MgII from the two samples after performing the two-sample K-S test ($p_{\text{KS}} = 0.23$), but the difference may exist in the distribution of FWHM-H β ($p_{\text{KS}} = 0.1$). For the distribution of 3000 Å versus 5100 Å luminosity, we found strong correlations for both of the two samples via the Spearman tests ($r = 0.92, p = 10^{-5}$ and $r = 0.75, p = 5 \times 10^{-5}$ for this work and Zuo15, respectively), supporting the consistency of the two continuum regions that are often used to estimate bolometric luminosities of quasars at high redshift.

To investigate the correlation in the distribution of BH mass versus Eddington ratio, we use the 16 BAL QSOs at $z < 4$ from our sample and compare them with three non-BAL QSO samples matched in luminosity and redshift (see Figure 7). Based on the two-sample K-S test, we cannot find a statistically significant difference in the distributions of Eddington ratio between the BAL and non-BAL samples; but potential differences may exist in the distribution of BH masses ($p_{\text{KS}} = 0.14$) between this work and Zuo15. Since the K-S test is incapable of finding any differences in the correlation strength between BH mass and Eddington ratio, and our sample appears to have no correlation in the distribution compared to apparent correlations over the three matched comparison samples, we perform the Spearman test to quantify this difference. As a result, we found strong correlations in all the three non-BAL comparison samples at a highly significant level compared to a tentative correlation in our sample (see Spearman test results in Figure 7).

The distributions of BH mass versus Eddington ratio above are unlikely biased because all of them are derived from the same BH mass estimator (H β), which is largely free of the effects of intrinsic reddening and absorption. In addition, the difference in the correlation strength between the non-BAL and BAL QSO samples is unlikely caused by the difference in sample size, as the V18 (blue) sample consisting of fewer QSOs, shows an even stronger correlation than those from C17 and our sample (Z15, C17, V18, and this work have 22, 19, 13, and 16 QSOs with H β -based BH masses, respectively).

4.1.1. Comparison with non-BAL QSO samples at lower luminosities

There are another two non-BAL QSO samples with available estimates of BH masses and Eddington ratios at $z \sim 4.8$, $z \sim 2.4$ and 3.3 (Trakhtenbrot et al. 2011; Netzer et al. 2007). Although the two sample have a lower luminosity range, they can provide additional diagnostics for systematic comparisons between the BAL and non-BAL populations.

In this subsection, we use the whole BAL sample rather than a subset for the investigations. Like our work, BH masses from all the three samples were estimated by the H β and MgII emission lines at $z < 4$ and $z > 4$, respectively. Note that the bolometric correction factor adopted in this work is about 1.5 times higher than that from the two non-BAL samples, we correct the distribution of bolometric luminosities by applying the same

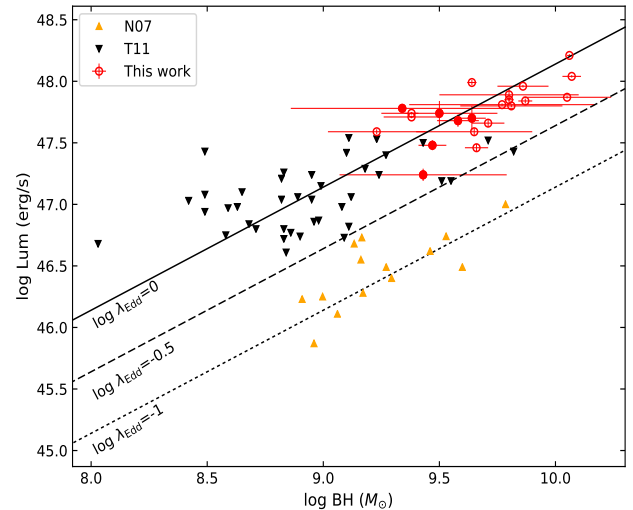


FIG. 8.— Distributions of bolometric luminosity versus BH mass for the three samples, where dotted, dashed, and solid black lines represent $\log \lambda_{\text{Edd}} = -1, -0.5, 0$, respectively. Filled red circles are LoBAL QSOs at $z > 4.3$ in our sample. It is clear that BAL QSOs on average do not have a higher Eddington ratio compared to the lower-luminosity sample of T11.

factor to the two comparison samples. As shown in Figure 8, there is a distinct separation between the two quasar subtypes, with on average larger BH mass in this work, which is quantitatively confirmed by a two-sample K-S test ($p_{\text{KS}} = 2 \times 10^{-8}$). This result is expected given apparently lower luminosities among the non-BAL QSOs from N07 and T11. Conversely, the vast majority of BAL QSOs in our sample are bounded by $\log \lambda_{\text{Edd}} = -0.5$ and $\log \lambda_{\text{Edd}} = 0.5$, with a median Eddington ratio of $\log \lambda_{\text{Edd}} = -0.04$. In addition, this median Eddington ratio is approximately equal to that from T11, consistent with the previous finding that higher redshift quasars tend to have higher Eddington ratios based on non-BAL samples, although our sample covers a higher luminosity range than that from T11.

There are six LoBAL QSOs at $z > 4.3$ in our sample (filled red circles in Figure 8) with their BH masses estimated by the MgII emission line. We compare the distributions of Eddington ratio between the six LoBAL QSOs and those of T11 sample since they are all measured by the MgII BH mass estimator. Based on the two-sample K-S test, we found that they are likely drawn from the same distribution ($p_{\text{KS}} = 0.9$). Therefore, in combination with the results from the comparison samples matched in luminosity and redshift (see the above section), our observational results together indicate that BAL QSOs on average do not have a higher Eddington ratio than that from non-BAL QSOs at similar luminosity and/or redshift.

4.2. Investigation of LoBAL QSOs

Urrutia et al. (2009) reported that there is an unusually high fraction of BAL/LoBAL QSOs at high redshift. In agreement with their finding, one of the conspicuous features of our sample is that at least half of them are LoBALs (see Table 2), and the LoBAL fraction becomes increasingly high at higher redshift ($z > 4.3$). Since LoBALs are ubiquitously hosted in strong BAL QSOs, we also add the QSO, J1032+5140 ($\text{EW} = 69.6 \text{ \AA}$ in C IV

TABLE 4

	L_{5100}^a	L_{5100}^b	FWHM- $H\beta^a$	FWHM- $H\beta^b$	λ_{Edd}
L_{3000}	$(0.92, 10^{-5})$	$(0.75, 5 \times 10^{-5})$	-	-	-
FWHM- Mg II	-	-	$(-0.09, 0.775)$	$(0.67, 0.0006)$	-
M_{BH}^a	-	-	-	-	$(0.552, 0.026)$
M_{BH}^b	-	-	-	-	$(0.831, 2 \times 10^{-6})$
M_{BH}^c	-	-	-	-	$(-0.637, 0.003)$
M_{BH}^d	-	-	-	-	$(-0.802, 9 \times 10^{-4})$

NOTE. — Spearman test results (r, p) of various distributions from different samples, in which a, b, c, d represent this work, Zuo15, C17, and V18, respectively.

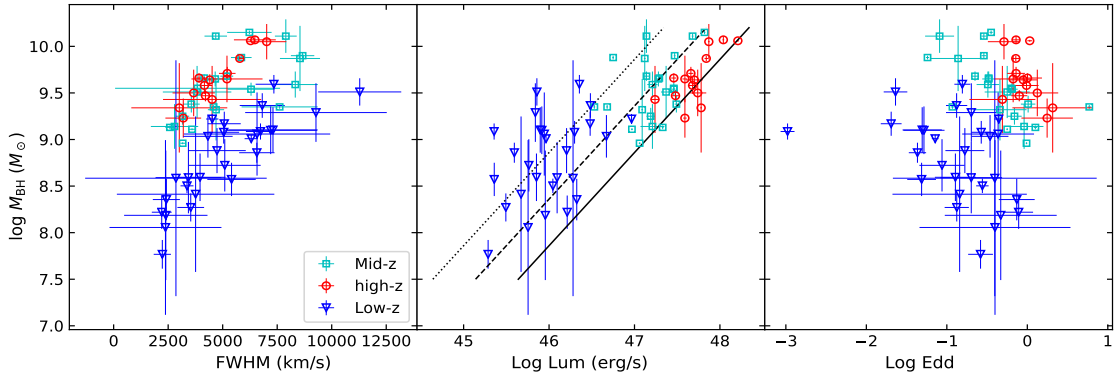


FIG. 9.— Distributions of BH mass versus FWHM (left), BH mass versus bolometric luminosity (middle), and BH mass versus Eddington ratio (right) in the three LoBAL samples, where dotted, dashed, and solid black lines represent $\log \lambda_{\text{Edd}} = -1, -0.5, 0$, respectively.

BAL), to the LoBAL subset for a systematic investigation.

On the other hand, we combine another two LoBAL samples for the investigation of the LoBAL population. One is from Schulze et al. (2017), where a uniform sample of 22 LoBAL QSOs at $1 < z < 2.5$ was constructed based on near-IR spectroscopy; the other was from Yi et al. (2019; accepted), which includes 36 LoBAL QSOs at $z < 1$ with BH masses estimated by the Balmer hydrogen emission line ($H\beta$ or $H\alpha$). These LoBAL samples based on consistent BH mass estimators provide comprehensive and complementary observational clues to advance our understanding with respect to the cosmological evolution in the LoBAL population (see Section 4.2.1). Since the three samples cover different redshift ranges (from $2.5 < z < 5$ to $1 < z < 2.5$ and $z < 1$), we mark them as high- z (red circles), mid- z (cyan squares), and low- z (blue triangles) BAL samples throughout this section.

Although we found the difference in correlation strength from the distribution of Eddington ratio versus BH mass between the BAL and non-BAL samples in section 4.1, a statistically significant conclusion cannot be drawn at this time due to a rather small sample size. Through the analysis of all the three LoBAL samples covering a wide redshift range, the relation between Eddington ratio and BH mass can be explored at a higher convincing level. After performing the Spearman tests, we found that only the mid- z sample shows a significant correlation; both low- z and high- z samples do not have significant correlations in the distribution of Eddington ratio versus BH mass, apparently different from previous studies based on non-BAL samples, where strong correlations are ubiquitously present (see Section 4.1). Therefore, the difference between composite spec-

tra (see Section 3.4) and the statistical results from the three LoBAL samples, support the argument of systematic differences between the BAL and non-BAL quasar populations. This may be caused by the effects of nuclear outflows traced by BALs and/or C IV broad emission-line blueshifts in the LoBAL subset. A dedicated future work is required to address this issue.

4.2.1. Redshift evolution in the LoBAL population

The distributions of redshift versus bolometric luminosity, BH mass, and Eddington ratio are shown in Figure 10. Clearly, the three samples cover a wide redshift range from $z \sim 0.5$ to $z \sim 5$, which can provide a unique joint and a complementary view of redshift evolution in the LoBAL population based on the consistent BH mass estimators ($H\beta$ and Mg II). Since these distributions have large scatters, we better characterize an overall trend using the median value in the redshift interval of $\Delta z = 1$. As a result, the three samples together show an increasing trend of Eddington ratio as the increase of redshift, while the distribution of BH mass appears to have a peak between $z = 3$ and $z = 4$. However, we caution that larger measurement uncertainties may exist for these BAL QSOs at $z > 4$ based on the Mg II emission line, as some of them suffer from partial absorption and/or continuum placement mentioned in Section 3.2. Most importantly, the apparent deficiency of LoBAL QSOs at $z > 4$ in our sample may bias the result. Therefore, a larger uniform sample based on the same BH mass estimator is required to confirm the peak in the distribution of BH mass versus redshift.

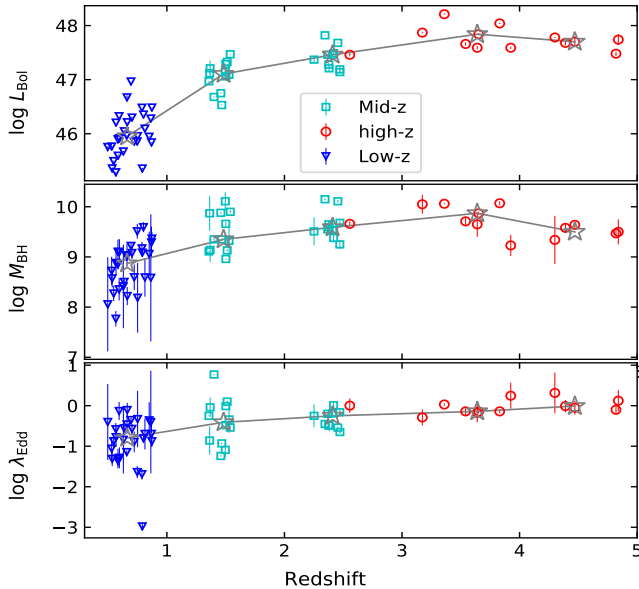


FIG. 10.— Distributions of redshift versus bolometric luminosity, BH mass and Eddington ratio in the three LoBAL samples. Grey stars and lines represent the median values and direct connections in each redshift interval of $\Delta z = 1$, respectively.

Combining the three samples above allows us to investigate the cosmological evolution ($0 < z < 5$) in the LoBAL population, provided the result is not much affected by the sample size and unevenly sampled data points within different redshift intervals.

At $z < 4$, these distributions are more reliable since their BH masses and Eddington ratios are measured by the Balmer emission-line estimator ($H\beta$ or $H\alpha$). To our surprise, both BH mass and Eddington ratio distributions appear to have an increasing trend as the increase of redshift at $z < 4$, obviously different from the trend seen in the two non-BAL QSO samples (N07 and T11), where BH mass/Eddington ratio decrease/increase as the increase of redshift (see Figure 8). Again, we caution that the results may be biased due to the decreasing number of LoBAL QSOs as the increase of redshift.

5. CONCLUSIONS

High- z BAL QSOs are a rare population, and they have been studied sparsely, usually only including individual objects or very small samples. In this work, we present a sample study of high-redshift BAL QSOs using optical/near-IR spectroscopy to investigate their statistical properties, mainly focusing on the distributions of luminosity, BH mass, and Eddington ratio, as well as their cosmological evolution in combination with the other two homogenous samples at $z < 1$ and $1 < z < 2.5$, respectively. Our main results are concluded as follows:

1. The composite spectra of these BAL QSOs characterized by deep and wide troughs in the sample were constructed, in which we see the prevalence of weak [O III] emission and large C IV emission-line blueshift ($\sim 3200 \text{ km s}^{-1}$), indicative of a special phase associated with strong nuclear outflows.
2. The 3000 \AA and 5000 \AA continuum luminosities show a strong correlation, consistent with previous

non-BAL QSO studies; however, there is no correlation between the Mg II and $H\beta$ lines in FWHM, probably due to the effects of nuclear outflows traced by BALs and/or C IV broad emission-line blueshifts.

3. Our observational results indicate that these high-redshift BAL QSOs on average do not have a higher Eddington ratio than that from non-BAL QSOs at similar luminosity and redshift.
4. There are no statistically significant differences either in the distribution of BH mass or in the distribution of Eddington ratio between the LoBAL and the matched non-BAL samples based on the two-sample K-S test results; however, we do find statistically significant differences in correlation strength from the distribution of BH mass versus Eddington ratio between the LoBAL and the matched non-BAL samples based on the Spearman test results (see Section 4.1).
5. There is an increasing trend in the distribution of Eddington ratio as a function of redshift from the augmented LoBAL sample at $0 < z < 5$, while the bolometric luminosity and BH mass distributions appear to peak at $3 < z < 4$, possibly reflecting the cosmological evolution path in the LoBAL QSO population.

Our investigations of 22 BAL QSOs at $3 \lesssim z \lesssim 5$, which consist of the largest such sample based on optical/near-IR spectroscopy in the redshift range ever studied. The observational results provide complementary and statistical insight into the BAL population with respect to the growth of SMBHs and physical properties of their central engines at high redshift, although a firm conclusion cannot be drawn in this work due to the limit in sample size. We require a significantly larger sample of high- z (Lo)BAL QSOs to confirm or improve the statistical results found in this work, by using the rest-frame UV/optical spectroscopy. However, it could be difficult to obtain such a sample in the next three or five years due to their rarity (particularly high- z LoBAL QSOs). Our spectroscopic investigations of high- z BAL QSOs covering the rest-frame UV/optical wavelengths therefore deliver the best statistical results to date.

W. Yi thanks the support from the National Science Foundation of China (NSFC-11703076) and the West Light Foundation of the Chinese Academy of Sciences (Y6XB016001). W. Yi also thanks the financial support from the program of China Scholarships Council (No. 201604910001) for his postdoctoral study at the Pennsylvania State University. This work is also supported by the Joint Research Fund in Astronomy (U1631127) under cooperative agreement between the National Science Foundation of China and Chinese Academy of Sciences.

We acknowledge the support of the staff of the Lijiang 2.4m telescope (LJT). Funding for the telescope has been provided by CAS and the People's Government of Yunnan Province. This research uses data obtained through the Telescope Access Program (TAP), which has been funded by the National Astronomical Observatories of

China, the Chinese Academy of Sciences (the Strategic Priority Research Program The Emergence of Cosmolog-

ical Structures Grant No. XDB09000000), and the Special Fund for Astronomy from the Ministry of Finance.

REFERENCES

- Allen, J. T., Hewett, P. C., Maddox, N., Richards, G. T., & Belokurov, V. 2011, *MNRAS*, 410, 860
- Becker, R. H., White, R. L., Gregg, M. D., et al. 2000, *ApJ*, 538, 72
- Bentz, M. C., Denney, K. D., Grier, C. J., et al. 2013, *ApJ*, 767, 149
- Bischetti, M.; Piconcelli, E.; Vietri, G. et al. 2017, *A&A*, 598, 122
- Boroson, T. A., & Green, R. F. 1992, *ApJS*, 80, 109
- Brotherton, M. S., Tran, H. D., Becker, R. H., et al. 2001, *ApJ*, 546, 775
- Coatman, L.; Hewett, P. C.; Banerji, M.; et al. 2017, *MNRAS*, 465, 21
- Cushing, M. C., Vacca, W. D., & Rayner, J. T. 2004, *PASP*, 116, 362
- Dai, X., Shankar, F., & Sivakoff, G. R. 2012, *ApJ*, 757, 180
- DiPompeo, M. A.; Brotherton, M. S.; Becker, R. H. et al. 2010, *ApJ*, 189, 83
- Fan, Y. F.; Bai, J. M.; Zhang, J. J. et al. 2015, *RAA*, 15, 918
- Farrar, D., Urrutia, T., Lacy, M., et al. 2010, *ApJ*, 717, 868
- Farrar, D., Urrutia, T., Lacy, M., et al. 2012, *ApJ*, 745, 178
- Faucher-Giguère, C.-A., Quataert, E., & Murray, N. 2012, *MNRAS*, 420, 1347
- Filiz Ak, N.; Brandt, W. N.; Hall, P. B. et al. 2013, *ApJ*, 777, 168
- Gallerani S.; Maiolino R.; Juarez Y., et al. 2010, *A&A*, 523, 85
- Gibson, R. R., Jiang, L., Brandt, W. N., et al. 2009, *ApJ*, 692, 758
- Grier, C. J.; Brandt, W. N.; Hall, P. B., et al. 2016, *ApJ*, 824, 130
- Hewett, P. C., & Foltz, C. B. 2003, *AJ*, 125, 1784
- Harrison, C. M., Alexander, D. M., Mullaney, J. R., & Swinbank, A. M. 2014, *MNRAS*, 441, 3306
- Irwin, M. J., Ibata, R. A., Lewis, G. F., & Totten, E. J. 1998, *ApJ*, 505, 529
- Jiang, L.; Fan, X.; Vestergaard, M. et al. 2007, *AJ*, 134, 1150
- Jeon, Y.; Im, M.; Kim, D. et al. 2017, *ApJS*, 231, 16
- Kaspi, S., Smith, P. S., Netzer, H., et al. 2000, *ApJ*, 533, 631
- López, S.; D’Odorico, V.; Ellison, S. L. et al. 2016, *A&A*, 594, 91
- Lazarova, M. S., Canalizo, G., Lacy, M., & Sajina, A. 2012, *ApJ*, 755, 29
- Margala, D., Kirkby, D., Dawson, K., et al. 2016, *ApJ*, 831, 157
- Maiolino, R., Oliva, E., Ghinassi, F., et al. 2004, *A&A*, 420, 889
- McLure, R. J., & Dunlop, J. S. 2004, *MNRAS*, 352, 1390
- Magain, P.; Surdej, J.; Swings, J.-P.; Borgeest, U.; Kayser, R. 1988, *Nature*, 334, 325
- Netzer, H., Shemmer, O., Maiolino, R., et al. 2004, *ApJ*, 614, 558
- Netzer, H., Lira, P., Trakhtenbrot, B., Shemmer, O., & Cury, I. 2007, *ApJ*, 671, 1256
- Pâris, I.; Petitjean, P.; Ross, N. et al. 2017, *A&A*, 597, 79
- Pei, Yichuan C., 1992, *ApJ*, 395, 130
- Plotkin, R. M.; Shemmer, O.; Trakhtenbrot, B., et al. 2015, *ApJ*, 805, 123
- Popovic, L. C.; Kovacevic-Dojcinovic, J.; Marceta-Mandic, S., 2019, *MNRAS*, 484, 3180
- Reichard T. A., Richards G. T.; Schneider D. P., et al. 2003a, *AJ*, 125, 1711
- Reichard T. A., Richards G. T.; Hall P. B., et al. *AJ*, 2003b, 126, 2594
- Salviander, S.; Shields, G. A.; Gebhardt, K.; Bonning, E. W., 2007, *ApJ*, 662, 131
- Schlafly, E. F.; Finkbeiner, D. P. 2011, *ApJ*, 737, 103
- Schulze, A.; Schramm, M.; Zuo, W. et al. 2017, *ApJ*, 848, 104
- Shen, Y., Richards, G. T., Strauss, M. A., et al. 2011, *ApJS*, 194, 45
- Trakhtenbrot, B., Netzer, H., Lira, P., Shemmer, O. 2011, *ApJ*, 730, 7
- Trakhtenbrot, B., & Netzer, H. 2012, *MNRAS*, 427, 3081
- Trump, J. R.; Hall, P. B.; Reichard, T. et al. 2006, *ApJS*, 165, 1
- Urrutia, T., Lacy, M., Spoon, H., et al. 2012, *ApJ*, 757, 125
- Urrutia, T., Becker, R. H., White, R. L., et al. 2009, *ApJ*, 698, 1095
- Vanden Berk, D. E.; Richards, G. T.; Bauer, A. et al. 2001, *AJ*, 122, 549
- Vestergaard, M., & Peterson, B. M. 2006, *ApJ*, 641, 689
- Violino, G., Coppin, K. E. K., Stevens, J. A., et al. 2016, *MNRAS*, 457, 1371
- Voit, G. M., Weymann, R. J., & Korista, K. T. 1993, *ApJ*, 413, 95
- Vietri, G.; Piconcelli, E.; Bischetti, M. et al. 2018, *A&A*, 617, 81
- Wang, Feige; Wu, Xue-Bing; Fan, X. et al. 2016, *ApJ*, 819, 24
- Weymann, R. J., Morris, S. L., Foltz, C. B., & Hewett, P. C. 1991, *ApJ*, 373, 23
- Wilson, J. C., Henderson, C. P., Herter, T. L., et al. 2004, *Proc. SPIE*, 5492, 1295
- Wang, F.; Fan, X.; Yang, J., et al. 2018, *ApJ*, 869, 9
- Woo, J.-H.; Le, H. Anh N.; Karouzos, M. et al. *ApJ*, 859, 138
- Yi, W., Wu, X., Wang, F., et al. 2015, *SCPMA*, 58, 5685
- Yi, W.; Green, R. F.; Bai, J.-M. et al. 2017, *ApJ*, 838, 135
- Yi, W.; Vivek, M.; Brandt, W. N., et al. 2019, *ApJ*, 870, 25
- Zuo, W., Wu, X.-B., Fan, X., et al. 2015, *ApJ*, 799, 189